

Adapting source grid parameters to improve the condition of the magnetostatic linear inverse problem of estimating nanoparticle distributions

Roland Eichardt · Daniel Baumgarten ·
Bojana Petković · Frank Wiekhorst ·
Lutz Trahms · Jens Haueisen

Received: 19 March 2012 / Accepted: 22 August 2012 / Published online: 13 September 2012
© International Federation for Medical and Biological Engineering 2012

Abstract The problem of estimating magnetic nanoparticle distributions from magnetorelaxometric measurements is addressed here. The objective of this work was to identify source grid parameters that provide a good condition for the related linear inverse problem. The parameters investigated here were the number of sources, the extension of the source grid, and the source direction. A new measure of the condition, the ratio between the largest and mean singular value of the lead field matrix, is proposed. Our results indicated that the source grids should be larger than the sensor area. The sources and, consequently, the magnetic excitation field, should be directed toward the Z-direction. For underdetermined linear inverse problems, such as in our application, the number of sources affects the condition to a relatively small degree. Overdetermined magnetostatic linear inverse problems, however, benefit from a reduction in the number of sources, which considerably improves the condition. The adapted source grids proposed here were used to estimate the magnetostatic dipole from simulated data; the L2-norm, residual, and

distances between the estimated and simulated sources were significantly reduced.

Keywords Magnetic nanoparticles · Particle imaging · Adaptation of source space grids · Condition number · Linear inverse problems

1 Introduction

Magnetic nanoparticles are in the focus of research in many biomedical applications [17, 19]. To reveal the location and the distribution of such particles, magnetorelaxometric measurements using SQUID sensor systems and linear inversion techniques can be used [3]. The imaging of magnetic nanoparticles is particularly important for hyperthermia cancer treatment [6, 23, 24] and for magnetic drug targeting [2, 4, 16].

To estimate the distributions of magnetic nanoparticles, the linear inverse problem (IP) of reconstructing dipole moments \mathbf{m} from a measured magnetic field \mathbf{b} has to be solved,

$$\mathbf{b} = \mathbf{L}\mathbf{m}. \quad (1)$$

The lead field matrix \mathbf{L} incorporates information about the sensor, source, and forward models. The lead field condition is crucial for the stability of the solution \mathbf{m} , in the presence of numerical errors and noise contained in \mathbf{b} . Our objective is to identify parameters associated with the source space grids to support a good condition for \mathbf{L} with respect to practical requirements. As a result, the linear inverse solution \mathbf{m} should be less sensitive to noise and errors. Because the condition is a property of the linear inverse problem (1), our findings are relevant to the application of different solution approaches, such as the TSVD [14], sLORETA [20], or FOCUSS [12] methods.

R. Eichardt (✉) · D. Baumgarten · B. Petković · J. Haueisen
Institute of Biomedical Engineering and Informatics,
Ilmenau University of Technology, P.O. Box 100565,
98684 Ilmenau, Germany
e-mail: Roland.Eichardt@tu-ilmenau.de

D. Baumgarten
Center for Biomedical Engineering, Universiti Teknologi
Malaysia, Johor, Malaysia

F. Wiekhorst · L. Trahms
Physikalisch-Technische Bundesanstalt, Berlin, Germany

J. Haueisen
Biomagnetic Center, Jena University Hospital, Jena, Germany

2 Methods

2.1 Sensor arrays and source spaces

Five sensor models of two magnetometer arrays, as typically used in magnetic nanoparticle measurements, were created. The first array represents the 304 channel PTB vector magnetometer system (Physikalisch-Technische Bundesanstalt, Berlin, Germany [22]), which we tested in four configurations: ‘PTB 304ch’ contained all 304 sensors, ‘PTB 114ch’ included the lowest 114 sensors with $Z < 0.5$ cm, ‘PTB 190ch’ included sensor layers with $Z < 3.5$ cm, and ‘PTB 247ch’ included sensor layers with $Z < 7.5$ cm. The AtB sensor system Argos 200 (Advanced Technologies Biomagnetics, Pescara, Italy) was used with 195 sensors, ‘ATB 195ch’.

The axes of the coordinate system are denoted X , Y , and Z . The axes were defined with respect to the sensor systems, in which the lowest sensors were positioned in the XY -plane with $Z = 0$. The positive Z -axis was upwardly directed from the center of the lowest sensors (see Fig. 1). The units corresponding to the positions and lengths are given in meters, if not stated otherwise. The term $\|\cdot\|$ describes the L2-norm.

Regular planar grids of magnetostatic dipoles were used to model the source space. The distance between the lowest sensor plane and the source space grid was 6 cm, which represented a typical distance between the sensor system and the nanoparticles in our application. When defining the source space grids, we used the following default values: the number of sources was defined to be $25 \times 25 = 625$, and the source grid area was configured with the dimensions 0.28×0.28 m², including an extension of 2 cm beyond the sensor area in both the X and Y directions. The centers of the source space grids were located at $X = Y = 0$, equivalent to the X/Y -centers of the sensor arrays. The standard direction of a source dipole was $+Z$. The sensor positions and directions of the array ‘PTB 304ch’ and the default source space grid are illustrated in Fig. 1.

The lead field matrix \mathbf{L} is a linear mapping from the source onto the sensor space and incorporates the source, sensor, and forward models. When considering a magnetostatic field (see, for instance Clark et al. [7, Chap. 10.1]), \mathbf{L} can be computed for sensor i and source j according to

$$\mathbf{L}(i,j) = \sum_k w_{ik} \mathbf{d}_i \cdot \frac{\mu_0}{4\pi} \left(\frac{3\mathbf{e}_j \cdot \mathbf{r}_{ijk}}{\|\mathbf{r}_{ijk}\|^5} \mathbf{r}_{ijk} - \frac{\mathbf{e}_j}{\|\mathbf{r}_{ijk}\|^3} \right),$$

where k are the indices corresponding to the sensor integration points, w are the sensor weights, \mathbf{d} are the sensor directions, \mathbf{e} are the source directions, and \mathbf{r} are the displacement vectors connecting the source positions and

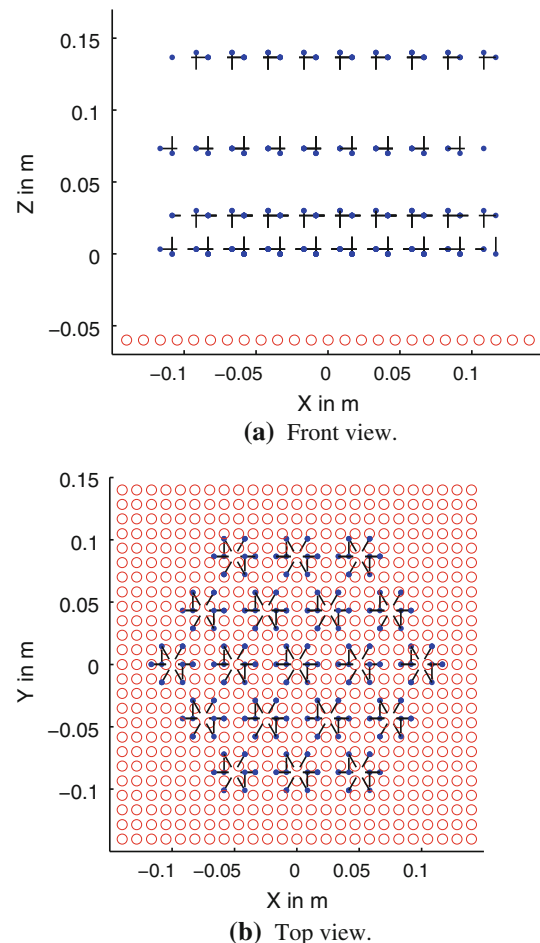


Fig. 1 Sensor positions (dots) and directions (bars) of the sensor array ‘PTB 304ch’. The default dipole positions of the source space grid are indicated by the circles

sensor integration points. The forward problem is solved for a given set of source activities \mathbf{m} by multiplying \mathbf{Lm} .

2.2 Condition measures

The condition of a lead field matrix \mathbf{L} can be analyzed using the condition number with respect to the L2-norm (e.g., [21, 11]). The condition number κ for $\mathbf{L} \neq 0$ is defined by

$$\kappa(\mathbf{L}) = \|\mathbf{L}\| \|\mathbf{L}^+\| = \sigma_1(\mathbf{L})\sigma_n(\mathbf{L})^{-1}, \quad (2)$$

where σ_i is the i th of n singular values (SVs) of \mathbf{L} , with $\sigma_1 > 0$ and $\sigma_i \geq \sigma_{i+1} \geq 0$. However, significant numerical errors can occur during the computation of κ (see Sect. ‘Accuracy of the condition number κ ’ of the Appendix), and κ depends essentially on the smallest SV σ_n .

To increase the numerical stability during evaluation of the condition of $\mathbf{L} \neq 0$ and to reduce its dependency on the smallest SV σ_n , we propose a new condition measure, ρ , in which

$$\rho(\mathbf{L}) = \frac{\sigma_1(\mathbf{L})}{1/n \sum_{i=1}^n \sigma_i(\mathbf{L})} = \left(\frac{1}{n} \sum_{i=1}^n \frac{\sigma_i(\mathbf{L})}{\sigma_1(\mathbf{L})} \right)^{-1}. \tag{3}$$

ρ represents the ratio between the largest and the mean SV of \mathbf{L} , as defined in the first part of Eq. (3). ρ can equivalently be interpreted as the inverse of the average decay of the SVs, as given in the second part of (3). A direct graphical comparison of the SV decay was presented by Nalbach et al. [18] as a measure for the information content of different sensor arrays. When a lead field matrix exhibits a slow decay of SVs, the correlations among the matrix rows (relate to the sensors) and among the matrix columns (relate to the sources) are small. Hence, the rows contain little redundant sensitivity information on the sources and, in practice, the information content of measurements provided by the modeled sensor array on the considered source distribution is high.

By employing the mean value of all SVs, the influence of the comparatively small SVs on ρ is considerably reduced. Smaller values of ρ and κ indicate a better condition in the context of \mathbf{L} and related linear inverse problems. In Sect. “Condition of the TSVD-regularized linear inverse problem” of the Appendix, we define $\rho_{\text{tsvd}}(\mathbf{L}, r)$ and $\kappa_{\text{tsvd}}(\mathbf{L}, r)$ to measure the condition of \mathbf{L} by considering the first r SVs only. Using this approach, we can determine the condition of TSVD-regularized [14] linear inverse problems, in which SVs smaller than σ_r are truncated. Practically relevant or optimal values of r , however, are often not known in advance. Further, we show in the Appendix sections “Condition of the TSVD-regularized linear inverse problem” and “Proof of $1 \leq \rho_{\text{tsvd}} \leq \rho$ ” that ρ_{tsvd} and κ_{tsvd} are bounded above by ρ and κ , respectively.

2.3 Simulations

In four simulations, the influence of the number of sources, grid extension, and dipole directions on the condition of the linear inverse problem, as measured by $\rho(\mathbf{L})$, were evaluated. In a fifth simulation, the relative improvements in the linear inverse solutions were measured using source space grids that were expected to provide an improved condition.

In simulation 1, we investigated the influence of the number of sources contained in the source space grid on ρ . The number of sources and dipoles, respectively, increased from $5 \times 5 = 25$ to $50 \times 50 = 2,500$. During this process, the source grid extensions and dipole directions were held constant at their default values.

The objective of simulation 2 was to vary the extensions of the source space grid relative to the sensor area in both the X and Y directions from -0.08 m (smaller than the sensor area) to $+0.12$ m (larger than the sensor area).

Simulation 3 combined simulations 1 and 2 by simultaneously evaluating the effect of the number of sources and the source grid extension on ρ .

In simulation 4, we gradually changed the uniform directions of the dipolar sources in the grid from 0° (the Z -direction) to 90° (the X -direction).

In simulation 5, we investigated the effects of adapted source grids on the quality of the linear inverse solutions. For this purpose, four exemplary source grids (A_1, A_2, B_1 , and B_2) were evaluated. This set consisted of two pairs of comparable grids, labeled with indices 1 and 2 that provided identical numbers of sources. Source grids B provided X/Y extensions and source directions, which were expected to improve the condition of the related linear IP. The parameters associated with the source grids A_1 – B_2 are given in Table 1.

Simulation 5 included one magnetostatic dipole with a moment of 1 nA m^2 at position $\mathbf{p}_0 = [-0.001, -0.001, -0.065]$. The dipole was directed toward $+Z$ for the source grids B and toward $+X$ for the source grids A , which corresponded to the assumed directions of the sources in the grid. The sensor array ‘PTB 304ch’ was used to simulate the measurement data, and white Gaussian noise with an SNR of 5 dB relative to the signal level of the dipole oriented toward $+X$ was added. For each grid, 100 simulation runs using different random noise profiles were performed.

The linear inverse problem was solved by applying the truncated singular value decomposition (TSVD) method [14]. The quality of the TSVD solutions was evaluated by testing all possible SV regularization parameters r , with $1 \leq r \leq n = 304$. In this process, n^{Dopt} counted the quantity of parameters r that resulted in solutions with a maximum dipolar moment located at the grid position $[0, 0, -0.6]$. This position in all four source grids represented the minimum distance to the simulated dipole and, therefore, the lowest localization error.

Furthermore, we compared the relative improvements (RI) of the solutions \mathbf{m}_r^B using the source grids B with solutions \mathbf{m}_r^A for grid A . To determine the RI, source grids with the same number of sources were compared, i.e., A_1 with B_1 and A_2 with B_2 . The individual relative

Table 1 Parameters that define the source space grids

Source grid	Number of grid points	X/Y source grid size in m^2	Directions of source dipoles
A_1	$25 \times 25 = 625$	0.2×0.2	$+X$
B_1	$25 \times 25 = 625$	0.28×0.28	$+Z$
A_2	$55 \times 55 = 3,025$	0.2×0.2	$+X$
B_2	$55 \times 55 = 3,025$	0.28×0.28	$+Z$

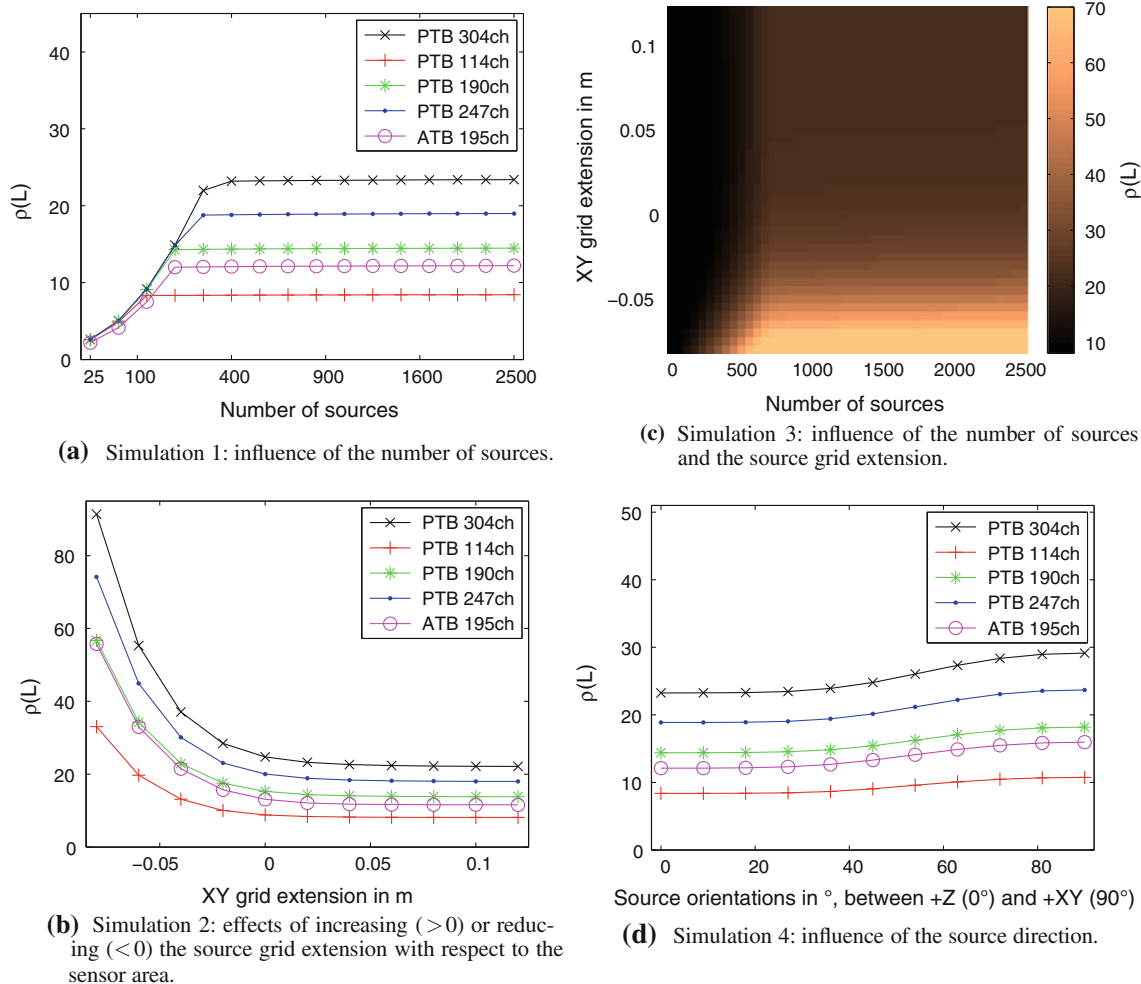


Fig. 2 Results of simulations 1–4. Lower values of ρ indicate a better condition

improvements in the solutions \mathbf{m}_r^B compared with \mathbf{m}_r^A were averaged over all possible TSVD regularization parameters r to yield a general measure that did not depend on the choice of r . The RI was evaluated with respect to the residual, RI^{Res} , the distance between the grid dipole and the highest estimated moment, the position of the simulated dipole, RI^{Dopt} , and the L2-norm of the solution, RI^{L2} . The residual and L2-norm of the solutions should be small, because their combined minimization is the objective of the TSVD minimum-L2-norm method.

To compare the solutions from grids B and A , the RI quantities were determined as follows:

$$RI^{Res}(B, A) = \frac{1}{n} \sum_{r=1}^n \frac{\|\mathbf{b} - \mathbf{L}_A \mathbf{m}_r^A\|}{\|\mathbf{b} - \mathbf{L}_B \mathbf{m}_r^B\|}, \tag{4}$$

$$RI^{Dopt}(B, A) = \frac{1}{n} \sum_{r=1}^n \frac{\|\mathbf{p}_0 - \mathbf{p}_{\max}(\mathbf{m}_r^A)\|}{\|\mathbf{p}_0 - \mathbf{p}_{\max}(\mathbf{m}_r^B)\|}, \tag{5}$$

$$RI^{L2}(B, A) = \frac{1}{n} \sum_{r=1}^n \frac{\|\mathbf{m}_r^A\|}{\|\mathbf{m}_r^B\|}. \tag{6}$$

The term $\mathbf{p}_{\max}(\mathbf{m}_r)$ in Eq. (5) represents a 3-by-1 vector that provides the source position with the maximum absolute value among all estimated dipole moments in \mathbf{m}_r . Among the three measures of RI, higher values indicate higher improvements and, therefore, better solutions. The TSVD solution \mathbf{m}_r using the regularization parameter r was computed according to

$$\mathbf{m}_r = \sum_{i=1}^r (\mathbf{u}_i^T \cdot \mathbf{b}) \sigma_i^{-1} \mathbf{v}_i, \tag{7}$$

where \mathbf{u} , σ , and \mathbf{v} are the singular vectors and values of the decomposition of the respective lead field, \mathbf{L} .

3 Results

The results of *simulation 1*, as shown in Fig. 2a, indicated that for an overdetermined IP ρ increased significantly for increasing numbers of sources. An underdetermined IP, however, yielded only a slight increase in ρ for an increase in the number of sources.

Table 2 Results of simulation 5: ρ , κ , and n^{Dopt}

Source grid	ρ	κ	Mean (n^{Dopt})
A_1	35.21	$2.71\text{e}+13$	22.0 ± 6.66
B_1	23.25	$2.01\text{e}+11$	62.3 ± 10.04
A_2	35.80	$2.05\text{e}+13$	7.7 ± 4.21
B_2	23.40	$1.98\text{e}+11$	34.2 ± 9.66

Figure 2b shows the results of simulation 2, which revealed that a larger source area decreased the measure ρ . Source space grids with extensions clearly smaller than the sensor area impaired the condition considerably. Positive extensions of the source grid beyond the sensor area led to a reduction in ρ .

The results of simulation 3 for the sensor array ‘PTB 304ch’ are shown in Fig. 2c. The influence of both parameters, the number of sources, and the extension of the grid in the X/Y directions were evaluated simultaneously. Almost no differences in ρ were observed for a grid extension of ≥ 2 cm and a number of sources equal to or greater than twice the number of sensors. As shown in simulations 1 and 2, ρ increased considerably for grid extensions that were clearly smaller than the sensor area, and ρ was low if the number of sources was less than the number of sensors.

The outcomes of simulation 4, shown in Fig. 2d, indicate that the dipolar sources should be oriented toward +Z to provide low values of ρ . Deviations in the source directions of more than 35° away from Z clearly increased the values of ρ .

Table 2 and Figs. 3, 4 and 5 show the results of simulation 5. The semi-logarithmic plots of the SVs for the lead field matrices using source grids A_2 and B_2 are illustrated in Fig. 3. The largest, mean, and smallest SVs are indicated by horizontal lines for both matrices. This plot shows that grid B_2 led to a better condition in terms of ρ and κ compared with A_2 because grid B_2 provided a smaller maximum SV together with higher values for the mean and smallest SVs.

Table 2 shows the condition measures ρ and κ for each of the four source grids A_1 – B_2 . The mean value of n^{Dopt} quantified the number of regularization parameters that led to inverse solutions with a minimum distance to the simulated dipole. Use of the grid B_1 instead of A_1 improved the lead field condition; ρ decreased by a value of 12 and κ decreased by a factor of 100. With the source grid A_1 , only 22 of 304 (7.2%) regularization parameters, on average, provided the lowest achievable localization error. With the source grid B_1 , 62 of 304 (20.5%) possible parameters r , on average, led to solutions with minimum localization errors. A comparison of the denser source grids A_2 and B_2 , which included 3,025 magnetostatic dipoles, revealed similar

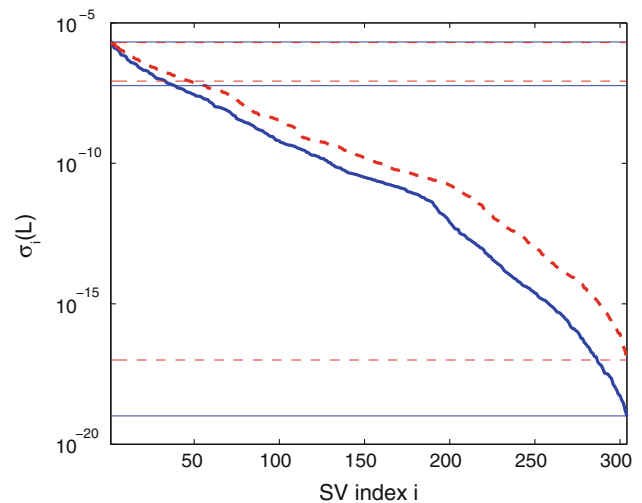


Fig. 3 Semi-logarithmic plot of the SVs of the lead field matrices using the ‘PTB 304ch’ sensor system and the source grids A_2 (blue solid lines) and B_2 (red dashed lines). The largest, mean, and smallest SVs are indicated by thin horizontal lines (color figure online)

improvements in ρ and κ when using grid B_2 instead of A_2 . With the source grid A_2 , 7.7 of 304 (2.5%) regularization parameters, on average, provided solutions with a minimum distance to the simulated dipole. The use of grid B_2 increased this number to 34.2 (11.3%).

The individual results for RI^{Res} , RI^{Dopt} , and RI^{L^2} of simulation 5 are shown in Fig. 4. The average relative improvements gained upon use of source grid B_1 instead of A_1 (Fig. 4a) are for RI^{Res} at 1.4, for RI^{Dopt} at 3.0, and for RI^{L^2} at 26.4. A comparison of the TSVD solutions using source grids B_2 and A_2 (Fig. 4b) yielded slightly lower mean relative improvements: RI^{Res} at 1.3, RI^{Dopt} at 3.0, and RI^{L^2} at 23.0. The variations in RI were relatively small over the 100 runs with different representations of white Gaussian noise. No run provided values with $\text{RI} \leq 1$.

Figure 5 shows the visually selected best TSVD solutions with the fewest artifacts and minimum distance between the strongest estimated source and the simulated dipole for grids A_1 – B_2 . The results for grids A (Fig. 5a, c) were obtained using the regularization parameter $r = 28$. For grids B, the best TSVD results were obtained using the regularization parameter $r = 40$ (Fig. 5b, d). Hence, the best estimates using grids B were provided by the larger parameters r . The differences between the solutions obtained using parameters between $r = 28$ and 40 were relatively small for B. The source grids B clearly provided fewer artifacts than the grids A, and the area of the highest source activity was more symmetric and focal. The results obtained using source grids with 625 and 3,025 sources differed not significantly. Application of the TSVD method to the source grids A_2 and B_2 , with 3,025 magnetostatic dipoles, resulted in smoother estimates with dipole

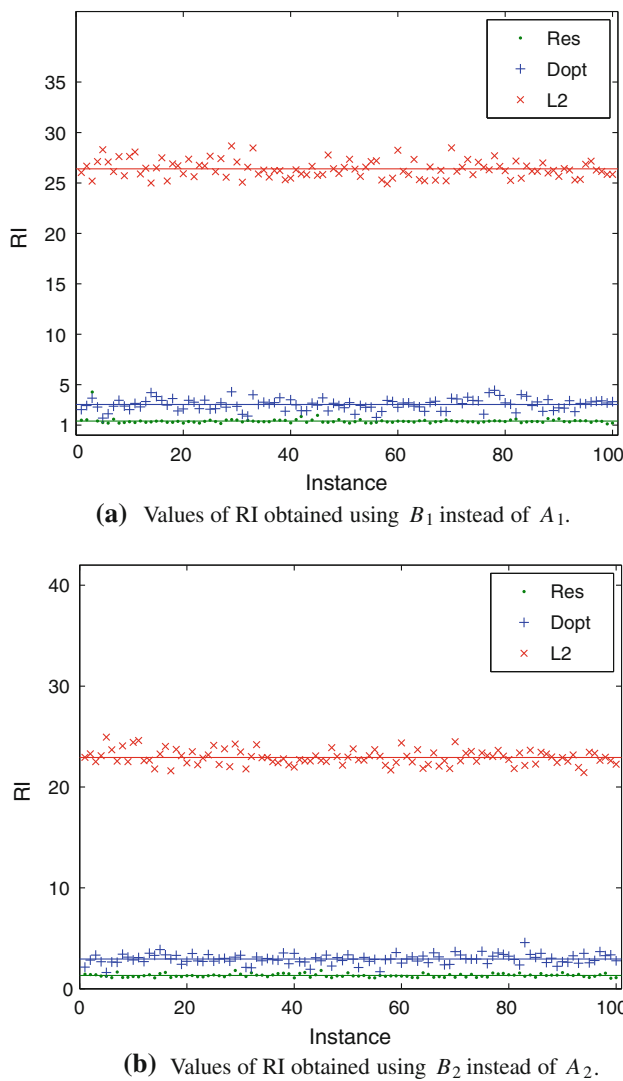


Fig. 4 Relative improvements in RI^{Res} (green dot), RI^{Dopt} (blue +), and RI^{L^2} (red \times). Individual results from 100 simulation runs using different representations of noise are shown. The mean RI values are indicated by horizontal lines. Higher ordinate values represent higher improvements obtained using grids B instead of A (color figure online)

moments that were a factor of 5 smaller than those obtained using A_1 and B_1 .

4 Discussion

The IP in our application is typically underdetermined; therefore, the number of sources produces a relatively small effect on the lead field condition. However, the practical application of a sparse source grid with equal or fewer numbers of sources than sensors can considerably improve the condition upon further reductions in the number of sources. The area of the source grid should

extend over the sensor area. Brauer et al. concluded previously, based on a phantom experiment, that a two-dimensional source space grid should extend over at least five times the area of the distributed source [5]. Accounting for the spatial resolution and the number of dipoles within the grid, an extension of 1–3 cm in each direction should be adequate, in practice.

The orientations of the sources in our application and, therefore, the direction of the magnetic field applied during excitation should not deviate more than 35° from the Z-direction. In addition, sources oriented toward Z also provided for the given sensor arrays higher signal levels and better SNRs.

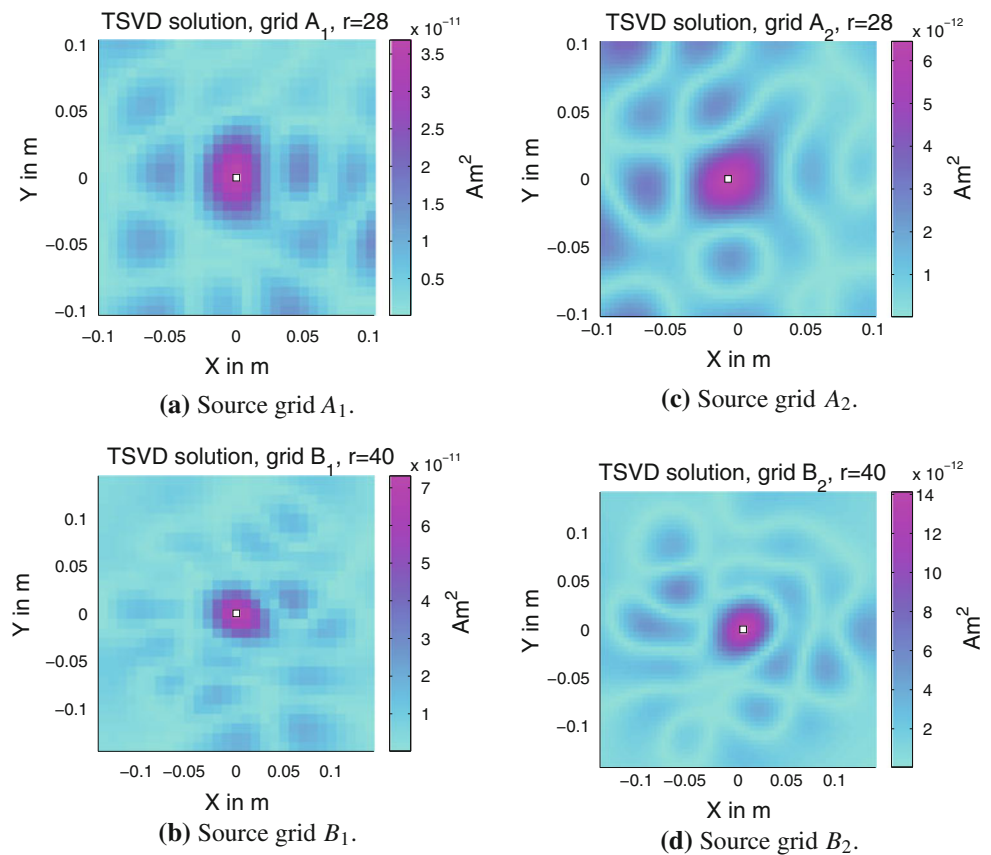
All five sensor array configurations in simulations 1–4 yielded qualitatively similar behavior that depended on the number of sensors. The best results for ρ were obtained for the configuration ‘PTB 114ch’. However, the better values of ρ obtained from the sensor array ‘PTB 114ch’, as compared with the values obtained from ‘PTB 304ch’, resulted mainly from the reduced number of SVs in the lead field matrix. A smaller number of sensors (as compared with the number of other arrays) introduce a relatively small redundancy in the measurement values; however, the ‘PTB 114ch’ sensor configuration picks up less information from the magnetic field compared to the configuration ‘PTB 304ch’.

As shown by the examples illustrated in simulation 5, the quality of the inverse solutions could be improved considerably using the source grid adaptations presented in this paper. Solutions using the adapted grids provided fewer artifacts, smaller L2-norms, and smaller residuals. In addition, a greater fraction of the possible TSVD regularization parameters led to optimal solutions in terms of the distance to the simulated source. Therefore, the appropriate determination of these parameters, for instance, using the Generalized-Cross-Validation [25] or the L-curve [13] methods should be easier and more reliable, in practice.

Some of our findings, including the specific recommendations for the source grid extensions and the direction of the magnetic sources, are directly related to the application of magnetic nanoparticle imaging. However, we expect that the basic findings, such as the general influence of the number of grid sources and the extensions of the source space on the lead field condition, are relevant to various linear IPs in magnetic applications. The findings of this study were used, for e.g., to detect ferromagnetic objects in geomagnetic measurements [10].

The condition measure, ρ , can be used to replace κ to reduce numerical errors that occur during the evaluation of the condition. In our example *simulation 5*, a shift in ρ by a value of 12 corresponded to a reduction in κ by a factor of 100. Variations in the parameters that define the source space grid yielded smooth changes in ρ , and ρ were not

Fig. 5 Plots of the visually best TSVD solutions showing the estimated magnetic moments of the dipoles defined by the source grid. The sources with the largest estimated moments are indicated by *square*



affected by obvious numerical errors. Furthermore, ρ can be used to evaluate the condition in other applications, e.g., to quantify the stability and convergence of the Newton method in finite element computations [26].

Acknowledgments We thank Uwe Graichen for his comments to the Appendix. This study was supported in part by the German Federal Ministry of Economics and Technology (KF2250108WD1) and by the German Research Foundation (GK 1567 and clinical research group KFO 213).

Appendix

Accuracy of the condition number κ

The singular value decomposition of the lead field matrices in this application was accomplished using the LAPACK’s DGESVD routine. Anderson et al. (section 4.9.1 of [1]) show that the DGESVD produces deviations in the computed SVs of $\hat{\sigma}_i$ relative to the true values σ_i , bounded by $\|\hat{\sigma}_i - \sigma_i\| \leq \epsilon\sigma_1$. (8)

The floating-point relative accuracy ϵ was $2.2e-16$ on the 64-bit systems used for our computations. Therefore, high relative accuracies of $\hat{\sigma}_i$ are only obtained for SVs close to σ_1 . Because the smallest SV σ_n is very small in relation to

σ_1 in this and many other applications, even low absolute errors in σ_n indicate high relative errors and lead to high absolute errors in σ_n^{-1} and κ .

Considering the definition (2), the accuracy of κ crucially depends on σ_n . Using the inequality (8), we obtain, for the relative error of σ_n

$$\frac{\|\hat{\sigma}_n - \sigma_n\|}{\sigma_n} \leq \frac{\epsilon\sigma_1}{\sigma_n} = \epsilon\kappa. \tag{9}$$

Consequently, the values of κ may be inaccurate, even in the order of magnitude, for $\kappa \geq \epsilon^{-1}$. Demmel [8] and Higham [15] stated that the condition number for computing the condition number is the condition number.

For special classes of matrices, it is feasible to compute all SVs, including the tiny SVs, with a high relative accuracy. An overview of this topic is provided by Demmel et al. [9]. This is not possible for general dense matrices, such as the lead field operators employed in our application.

Condition of the TSVD-regularized linear inverse problem

To facilitate stable linear inverse solutions, regularization methods are applied to improve the condition. For example, when computing a linear inverse solution using the

TSVD approach (7) and a regularization parameter r , with $1 \leq r \leq n$, all singular components with SVs smaller than σ_r are omitted. Depending on the parameter r , the TSVD regularization changes the linear IP and causes a regularization error, which should be smaller than the error that results from an inferior condition.

To measure the condition of the TSVD-regularized linear inverse problem for a lead field matrix \mathbf{L} , the definitions of κ and ρ , (2) and (3), are modified to consider the largest r SVs only:

$$\kappa_{\text{tsvd}}(\mathbf{L}, r) = \sigma_1(\mathbf{L})\sigma_r(\mathbf{L})^{-1}, \tag{10}$$

$$\rho_{\text{tsvd}}(\mathbf{L}, r) = \frac{\sigma_1(\mathbf{L})}{1/r \sum_{i=1}^r \sigma_i(\mathbf{L})} = \left(\frac{1}{r} \sum_{i=1}^r \frac{\sigma_i(\mathbf{L})}{\sigma_1(\mathbf{L})} \right)^{-1}. \tag{11}$$

From (2) and (10), we obtain for any r between 1 and n

$$1 \leq \kappa_{\text{tsvd}}(\mathbf{L}, r) \leq \kappa(\mathbf{L}), \tag{12}$$

and, from (3) and (11),

$$1 \leq \rho_{\text{tsvd}}(\mathbf{L}, r) \leq \rho(\mathbf{L}). \tag{13}$$

The property (12) follows because $\sigma_1 \geq \sigma_r \geq \sigma_n$. A proof for (13) is shown in Sect. ‘‘Proof of $1 \leq \rho_{\text{tsvd}} \leq \rho$ ’’ of the Appendix. According to (12) and (13), κ and ρ are the least upper bounds for κ_{tsvd} and ρ_{tsvd} . In practice, the optimal choice of r for a matrix \mathbf{L} and the resulting values of $\kappa_{\text{tsvd}}(\mathbf{L}, r)$ and $\rho_{\text{tsvd}}(\mathbf{L}, r)$ can vary widely.

Proof of $1 \leq \rho_{\text{tsvd}} \leq \rho$

To prove $1 \leq \rho_{\text{tsvd}}(\mathbf{L}, r) \leq \rho(\mathbf{L})$, we first show that $\rho_{\text{tsvd}}(\mathbf{L}, r)$ is smaller or equal $\rho(\mathbf{L})$ for all regularization parameters r between 1 and n :

$$\begin{aligned} \left(\frac{1}{r} \sum_{i=1}^r \frac{\sigma_i(\mathbf{L})}{\sigma_1(\mathbf{L})} \right)^{-1} &\leq \left(\frac{1}{n} \sum_{i=1}^n \frac{\sigma_i(\mathbf{L})}{\sigma_1(\mathbf{L})} \right)^{-1} \\ \iff \frac{1}{r} \sum_{i=1}^r \frac{\sigma_i(\mathbf{L})}{\sigma_1(\mathbf{L})} &\geq \frac{1}{n} \sum_{i=1}^n \frac{\sigma_i(\mathbf{L})}{\sigma_1(\mathbf{L})} \\ \iff n \sum_{i=1}^r \sigma_i(\mathbf{L}) &\geq r \sum_{i=1}^n \sigma_i(\mathbf{L}) \\ \iff r \sum_{i=1}^r \sigma_i(\mathbf{L}) + (n-r) \underbrace{\sum_{i=1}^r \sigma_i(\mathbf{L})}_{\geq r \times \sigma_r(\mathbf{L})} \\ &\geq r \sum_{i=1}^r \sigma_i(\mathbf{L}) + r \underbrace{\sum_{i=r+1}^n \sigma_i(\mathbf{L})}_{\leq (n-r) \times \sigma_{r+1}(\mathbf{L})} \\ \iff (n-r) \times r \times \sigma_r(\mathbf{L}) &\geq r \times (n-r) \times \sigma_{r+1}(\mathbf{L}) \\ \iff \sigma_r(\mathbf{L}) &\geq \sigma_{r+1}(\mathbf{L}) \end{aligned}$$

which is provided by the singular value decomposition of \mathbf{L} . Second, from $\sigma_1(\mathbf{L}) \geq \sigma_i(\mathbf{L})$ follows $r \times \sigma_1(\mathbf{L}) \geq \sum_{i=1}^r \sigma_i(\mathbf{L})$ and $1 \leq \rho_{\text{tsvd}}(\mathbf{L}, r)$. \square

References

1. Anderson E, Bai Z, Bischof C, Blackford S, Demmel J, Dongarra J, Du Croz J, Greenbaum A, Hammarling S, McKenney A, Sorensen D (1999) LAPACK users’ guide, 3rd edn. SIAM, Philadelphia, PA. <http://www.netlib.org/lapack/lug/>
2. Babinec P, Krafčík A, Babincová M, Rosenecker J (2010) Dynamics of magnetic particles in cylindrical halbach array: implications for magnetic cell separation and drug targeting. *Med Biol Eng Comput* 48(8):745–753. doi:10.1007/s11517-010-0636-8
3. Baumgarten D, Liehr M, Wiekhorst F, Steinhoff U, Münster P, Miethe P, Trahms L, Hauelsen J (2008) Magnetic nanoparticle imaging by means of minimum norm estimates from remanence measurements. *Med Biol Eng Comput* 46(12):1177–1185. doi:10.1007/s11517-008-0404-1
4. Bharali DJ, Mousa SA (2010) Emerging nanomedicines for early cancer detection and improved treatment: current perspective and future promise. *Pharmacol Ther* 128(2):324–335. doi:10.1016/j.pharmthera.2010.07.007
5. Brauer H, Hauelsen J, Ziolkowski M, Tenner U, Nowak H (2000) Reconstruction of extended current sources in a human body phantom applying biomagnetic measuring techniques. *IEEE Trans Magn* 36(4):1700–1705. doi:10.1109/20.877770
6. Cherukuri P, Glazer ES, Curley SA (2009) Targeted hyperthermia using metal nanoparticles. *Adv Drug Deliv Rev* 62(3):339–345. doi:10.1016/j.addr.2009.11.006
7. Clark J, Braginski AI (eds) (2006) The SQUID handbook, vol 2: applications of SQUIDS and SQUID systems. Wiley-VCH, New York
8. Demmel JW (1987) On condition numbers and the distance to the nearest ill-posed problem. *Numer Math* 51(3):251–289. doi:10.1007/BF01400115
9. Demmel JW, Gu M, Eisenstat S, Slapnicar I, Veselic K, Drmac Z (1999) Computing the singular value decomposition with high relative accuracy. *Linear Algebra Appl* 299:21–80. doi:10.1016/S0024-3795(99)00134-2
10. Eichardt R, Baumgarten D, Di Rienzo L, Linzen S, Schultze V, Hauelsen J (2009) Localisation of buried ferromagnetic objects based on minimum-norm-estimations—a simulation study. *Int J Comput Math Electron Electron Eng* 28(5):1327–1337. doi:10.1108/03321640910969566
11. Eichardt R, Hauelsen J (2010) Influence of sensor variations on the condition of the magnetostatic linear inverse problem. *IEEE Trans Magn* 46(8):3449–3453. doi:10.1109/TMAG.2010.2046149
12. Gorodnitsky IF, George JS, Rao BD (1995) Neuromagnetic source imaging with FOCUSS: a recursive weighted minimum norm algorithm. *Electroencephalogr Clin Neurophysiol* 95(4):231–251. doi:10.1016/0013-4694(95)00107-A
13. Hansen PC, O’Leary DP (1993) The use of the L-curve in the regularization of discrete ill-posed problems. *SIAM J Sci Comp* 14(6):1487–1503. doi:10.1137/0914086
14. Hanson RJ (1971) A numerical method for solving fredholm integral equations of the first kind using singular values. *SIAM J Numer Anal* 8(3):616–622. doi:10.1137/0708058
15. Higham DJ (1995) Condition numbers and their condition numbers. *Linear Algebra Appl* 214:193–213. doi:10.1016/0024-3795(93)00066-9

16. Jain KK (2010) Advances in the field of nanooncology. *BMC Med* 8:83. doi:[10.1186/1741-7015-8-83](https://doi.org/10.1186/1741-7015-8-83)
17. Lim C, Han J, Guck J, Espinosa H (2010) Micro and nanotechnology for biological and biomedical applications. *Med Biol Eng Comput* 48(10):941–943. doi:[10.1007/s11517-010-0677-z](https://doi.org/10.1007/s11517-010-0677-z)
18. Nalbach M, Dössel O (2002) Comparison of sensor arrangements of MCG and ECG with respect to information content. *Phys C* 372–376:254–258. doi:[10.1016/S0921-4534\(02\)00683-4](https://doi.org/10.1016/S0921-4534(02)00683-4)
19. Pankhurst QA, Thanh NKT, Jones SK, Dobson J (2009) Progress in applications of magnetic nanoparticles in biomedicine. *J Phys D Appl Phys* 42(22). doi:[10.1088/0022-3727/42/22/224001](https://doi.org/10.1088/0022-3727/42/22/224001)
20. Pascual-Marqui RD (2002) Standardized low resolution brain electromagnetic tomography (sLORETA): technical details. *Method Find Exp Clin Pharm* 24(D):5–12
21. Rouve LL, Schmerber L, Chadebec O, Foggia A (2006) Optimal magnetic sensor location for spherical harmonic identification applied to radiated electrical devices. *IEEE Trans Magn* 42(4): 1167–1170. doi:[10.1109/TMAG.2006.872016](https://doi.org/10.1109/TMAG.2006.872016)
22. Schnabel A, Burghoff M, Hartwig S, Petsche F, Steinhoff U, Drung D, Koch H (2004) A sensor configuration for a 304 SQUID vector magnetometer. *Neurol Clin Neurophysiol* 70. <http://www.neurojournal.com/article/view/284>
23. Su D, Ma R, Salloum M, Zhu L (2010) Multi-scale study of nanoparticle transport and deposition in tissues during an injection process. *Med Biol Eng Comput* 48(9):853–863. doi:[10.1007/s11517-010-0615-0](https://doi.org/10.1007/s11517-010-0615-0)
24. Su D, Ma R, Zhu L (2011) Numerical study of nanofluid infusion in deformable tissues for hyperthermia cancer treatments. *Med Biol Eng Comput* 49(11):1233–1240. doi:[10.1007/s11517-011-0819-y](https://doi.org/10.1007/s11517-011-0819-y)
25. Wahba G (1977) Practical approximate solutions to linear operator equations when the data are noisy. *SIAM J Numer Anal* 14(4):651–667. doi:[10.1137/0714044](https://doi.org/10.1137/0714044)
26. Weichert F, Schröder A, Landes C, Shamaa A, Awad S, Walczak L, Müller H, Wagner M (2010) Computation of a finite element-conformal tetrahedral mesh approximation for simulated soft tissue deformation using a deformable surface model. *Med Biol Eng Comput* 48(6):597–610. doi:[10.1007/s11517-010-0607-0](https://doi.org/10.1007/s11517-010-0607-0)